Nano Research

Open Access

Research Article

N-doped bamboo-like carbon nanotube-encapsulated CuNi alloy to enrich nitrate and boost electrochemical ammonia synthesis

Guohao Jia[2,§], Yuanqing Sun[1,2,§✉], Peilin Liu[2], Jiaqing Luo[3], Peng Zhang[4], Yuechang Wei[1,2], Weiyu Song[1,2], Zhenxing Li[1✉], Zhen Zhao[1,5], and Jian Liu[1,3✉]

[1] *State Key Laboratory of Heavy Oil Processing, China University of Petroleum, Beijing 102249, China*
[2] *College of Science, Beijing Key Laboratory of Oil and Gas Optical Detection Technology, and Basic Research Center for Energy Interdisciplinary, China University of Petroleum, Beijing 102249, China*
[3] *State Key Laboratory of Heavy Oil Processing at Karamay, China University of Petroleum Beijing at Karamay, Karamay 834000, China*
[4] *Petrochemical Research Institute, PetroChina Company Limited, Beijing 102206, China*
[5] *Institute of Catalysis for Energy and Environment, College of Chemistry and Chemical Engineering, Shenyang Normal University, Shenyang 110034, China*
[§] *Guohao Jia and Yuanqing Sun contributed equally to this work.*

Cite this article: *Nano Research*, **2025**, *18*, 94907265. https://doi.org/10.26599/NR.2025.94907265

ABSTRACT: Ammonia plays an irreplaceable role in agricultural production and also is an important chemical raw material and energy carrier. Developing a catalyst for the electrochemical NO_3^- reduction reaction (NO_3RR) to synthesize ammonia is crucial for energy, food security and pollution control. Herein, by adjusting the Cu/Ni ratio, we report a simple impregnation and calcination method to synthesize a N-doped bamboo-like carbon nanotube (CNT)-encapsulated CuNi alloy catalyst (Cu_7Ni_3-CNT). Cu_7Ni_3-CNT reveals an excellent ammonia synthesis performance, which has the highest Faraday efficiency (FE, 99.18%) at −0.8 V vs. reversible hydrogen electrode (RHE), along with an ammonia production rate of 20.90 $mg \cdot cm^{-2} \cdot h^{-1}$. In addition, the highest ammonia production rate of Cu_7Ni_3-CNT can reach 23.21 $mg \cdot cm^{-2} \cdot h^{-1}$, with a high FE (90.80%) at −1.0 V vs. RHE. At the same time, the electrocatalyst displays exceptional stability, which can operate steadily for 400 h at 300 $mA \cdot cm^{-2}$. The high catalytic activity and excellent stability derive from catalyst structure and the synergistic effect between Cu_7Ni_3 alloy and encapsulating bamboo-like CNT. The incorporation of Ni enhances the intrinsic activity of Cu for NO_3RR. CNT endows the catalyst with a larger specific surface area, more exposed active sites to further improve the apparent activity, and higher stability. The internal cavity of CNT also contributes to the enrichment of nitrate. Furthermore, *in-situ* Raman spectroscopy and density functional theory (DFT) calculations reveal that Cu in the alloy can effectively adjust the adsorption energy of $*NO_3$ by Ni element and increase the activity of *H as the reduction driving force, thereby improving the intrinsic activity of NO_3RR.

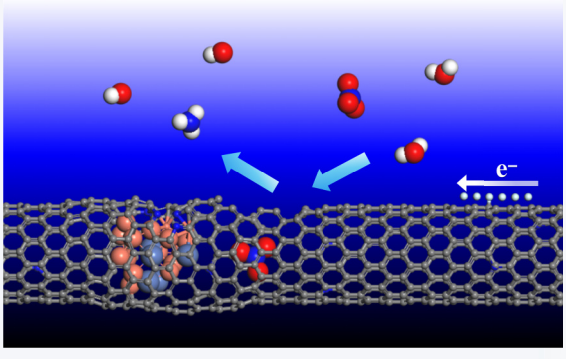

KEYWORDS: carbon nanotube, CuNi alloy, NO_3^- reduction reaction, ammonia synthesis, nitrate enriching

1 Introduction

Along with the progression of human activities and the economic society, the nitrification process, wherein nitrates are gradually oxidized from low-valent nitrogen species such as ammonia and nitrogen, is continuously intensified. This situation leads to a continuous increase in the concentration of nitrates in water bodies, which has gravely threatened the living environment of various organisms in nature [1]. Simultaneously, ammonia plays an irreplaceable role in agricultural production and also is an important chemical raw material and energy carrier [2]. In contrast to the currently mainstream Haber–Bosch process for ammonia synthesis [3], electrochemical nitrate reduction to synthesize ammonia (NO_3^- reduction reaction (NO_3RR)), which can be combined with clean energy sources such as wind energy and solar

Received: December 4, 2024; **Revised:** January 7, 2025
Accepted: January 20, 2025

✉Address correspondence to Yuanqing Sun, yqsun@cup.edu.cn; Zhenxing Li, lizx@cup.edu.cn; Jian Liu, liujian@cup.edu.cn

energy [4, 5], is an ideal ammonia synthesis process with lower energy consumption, greater cleanliness, and sustainability. Moreover, NO_3RR is not restricted by the high bond energy N≡N bonds of nitrogen [5], and the activation energy in the adsorption and activation process of nitrate ions is much lower [6]. Thus, NO_3RR is an efficient and environmentally friendly technology for removing excessive nitrates and synthesizing ammonia.

The mechanism of NO_3RR is relatively complex [7], which is generally believed that the active hydrogen species (H*) generated by Volmer step of hydrogen evolution reaction (HER) provide driving force in reduction reactions [3]. However, HER is also the main competitive reaction of NO_3RR. Hydrogen produced in Heyrovsky and Tafel step of HER should be avoided as much as possible [8]. Additionally, electrode potential [4] and the pH of the electrolyte [9] are also significant factors affecting the ammonia synthesis performance of catalysts. The active sites and substrates of the electrocatalyst can have a huge influence on the performance of NO_3RR.

Carbon is an important class of substrate materials widely used in the field of electrocatalysis with excellent electrical conductivity, strong ability to disperse metal active sites, and easy modification and decoration [10]. According to recent studies, structures of metal active sites encapsulated by carbon have been continuously synthesized, and the concept of "armor catalyst" has been proposed [11]. The carbon layer is considered to play a confinement role in inhibiting metal sintering during the process of catalyst synthesis and plays a vital role in balancing the hydrophilicity and hydrophobicity of the surfaces and significantly improving stability in electrochemical reactions [12–14]. However, in past studies, the mass transfer process of substances between the inside and outside of the carbon layer has not been accurately studied, especially for carbon nanotube (CNT).

In the electrocatalytic process, metals are typically regarded as the primary active sites. Compared with noble metal-based catalyst [15–17] and metal compound-based catalyst (such as CoP [18], Co_3O_4 [19], MXene [20], layered double hydroxide (LDH) [21], and MoS_2 [22]), non-noble metal catalyst, because of its higher activity, higher selectivity, and lower price, has become one of the research focuses of NO_3RR. Especially, the energy barrier of $NO_3^- \rightarrow NO_2^*$ on copper-based catalysts is much lower than that of other metal-based catalysts, making it a kind of ideal NO_3RR catalysts. According to recent studies, various types of Cu active sites, typically Cu-based nanoparticles (NPs), Cu-N_4 [23–25], CuO, and Cu_2O [26, 27], have been synthesized and compared, from which it is demonstrated that the intrinsic activity of Cu^0 is superior to that of Cu^{2+} and Cu^+. Hu et al. [28] discovered through theoretical calculations that the suppressed HER activity under alkaline conditions endowed Cu-based catalysts with better ammonia synthesis activity and selectivity. On this basis, compared with Cu (100) and the Cu (110), Cu (111) possessed better HER activity under alkaline conditions, resulting to a higher density of H*. Meanwhile, Cu (111) also exhibited better ability to adsorb and activate nitrate, thus having the best NO_3RR activity. In the meantime, incorporating other metals into metal nanoparticles to form an alloy structure is a common and vital means to improve the catalytic performance of metals. This can be attributed to the optimization of the metal electronic structure, the adsorption of species and the energy barriers associated with elementary reactions, which confer inherent advantages to alloys in catalytic processes.

It is well-known that copper readily forms a binary alloy structure with other metals [29]. There have been numerous studies on bimetallic alloy catalysts formed by Cu with noble metals [30, 31] or non-noble metals [32–34]. Recent researches have indicated that the addition of metal promoters can play roles in improving the dissociation ability of water on the Cu surface, promoting the generation of surface H* [35], adjusting the adsorption of nitrate by adjusting the electronic structure of Cu, and accelerating the desorption of ammonia [36, 37]. Wang et al. [38] found that CuNi alloy has the lowest limiting potential (−0.29 V) compared with other CuM (M represents other transition metals that serve as promoters to form alloys with Cu, such as, Fe, Co, Ni, Ag, Au, Ru, Pt, Pd, etc.) binary alloys, due to the greatly reduced reaction activation energy of the rate-controlling steps ($NO_3^- \rightarrow *NO_2$ and $*NO \rightarrow NHO*$) and the high-density H* generated by water dissociation on the (111) crystal plane of CuNi, corresponding to the best ammonia synthesis performance by theoretical calculations. Current literature on alloy catalysts predominantly focuses on the impact of carbon materials on metal active sites [39–41] and the regulatory role of metal atoms functioning as cocatalysts within metal alloys on those acting as active sites [42–44]. The effect of alloy nanoclusters on the morphology of carbon materials is rarely mentioned.

In the catalyst synthesis process, particularly when bimetallic alloy catalysts are produced through mixing and calcining metal precursors and carbon sources, the feeding ratio of the two metals not only affects the structure and activity of metal active sites but also inevitably influences the morphology and physicochemical properties of the carbon material itself [45]. Herein, we synthesized N-doped bamboo-like carbon nanotube encapsulated CuNi alloy with mixing and calcining metal precursors and carbon sources. By adjusting the ratio of Cu to Ni, the morphology of catalyst also changed significantly. *In-situ* Fourier transform infrared spectroscopy (FT-IR) revealed that nitrate entered the CNT through mesopores and micropores generated by carbon defects and enriched in the cavity of the CNT. At the same time, the introduction of Ni weakened the adsorption of nitrate on the Cu surface and increased the activity of H*, thereby significantly accelerating the hydrodeoxygenation process, especially reducing the energy barrier of the rate-controlling step ($*NH \rightarrow *NH_2$). Consequently, compared with other CuNi ratios, Cu_7Ni_3/CNT exhibited the best ammonia synthesis performance with a potential of −0.8 V vs. reversible hydrogen electrode (RHE), the ammonia synthesis rate and Faraday efficiency (FE) are as high as 20.90 $mg \cdot cm^{-2} \cdot h^{-1}$ and 99.18%, respectively. Furthermore, benefiting from the bamboo-like CNT protection, Cu_7Ni_3/CNT showed excellent stability which potential was decreased slightly after electrolysis for 400 h at a high current density of 300 $mA \cdot cm^{-2}$. In general, this study demonstrates that the precise adjustment of the CuNi ratio facilitates the formation of CNTs and optimizes both nitrate diffusion and the intrinsic activity and stability of alloy NPs.

2 Experimental section

2.1 Materials and chemicals

Potassium hydroxide (KOH, 99%), melamine ($C_3H_6N_6$, 99%) and nickel chloride hexahydrate ($NiCl_2 \cdot 6H_2O$, 99%) were purchased by Shanghai Macklin Biochemical Technology Co., Ltd. Ethanol (C_2H_5OH, 99.5%) was purchased from Beijing Tong Guang Fine Chemicals Company. Ammonium sulfate ($(NH_4)_2SO_4$, 99%), ammonium sulfate-^{15}N ($(^{15}NH_4)_2SO_4$, 99%, isotopic abundance: 10 at.%), copper chloride dihydrate ($CuCl_2 \cdot 2H_2O$, 99%), potassium

nitrate (KNO_3, 99%) and potassium nitrate-^{15}N ($K^{15}NO_3$, 99%, isotopic abundance: 10 at.%) were purchased from Shanghai Aladdin Biochemical Technology Co., Ltd. Nafion perfluorinated resin (5 wt.%) was purchased from Shanghai Titan Technology Co., Ltd. Carbon paper (CP, 1 mm) was purchased from Suzhou Sinero Technology Co., Ltd.

2.2 Synthesis of Cu_7Ni_3-mel

1.427 mmol of $CuCl_2{\cdot}2H_2O$ and 14.27 mmol of $NiCl_2{\cdot}6H_2O$ (molar ratio, n_{Cu}:n_{Ni} = 1:10) were dissolved in 50 mL of deionized water. 6 g of melamine were dispersed into 250 mL of ethanol with magnetic stirring for 30 min until mixing evenly. The aqueous solution was added to the suspension, and the mixture was stirred for 12 h. Afterwards, the sediment was centrifuged, washed with ethanol, and dried.

2.3 Synthesis of Cu_7Ni_3/CNT

1 g as-prepared Cu_7Ni_3-mel and 5 g melamine were ball-milled evenly and then annealed at 800 °C in an argon atmosphere with a ramping rate of 5 °C·min^{-1} for 4 h.

2.4 Synthesis of Cu_xNi_{10-x}/CN

The feed molar ratio of $CuCl_2{\cdot}2H_2O$ and $NiCl_2{\cdot}6H_2O$ was changed (1:1, 1:5, 1:12, and 1:15) to synthesize Cu_xNi_{10-x}-mel, and then Cu_xNi_{10-x}/CN (x = 9, 8, 6, and 5).

2.5 Synthesis of Cu/CN and Ni/CN

Using a similar synthesis method, $CuCl_2{\cdot}2H_2O$ or $NiCl_2{\cdot}6H_2O$ was added to synthesize Cu-mel and Ni-mel, and then Cu/CN and Ni/CN.

2.6 Preparation of the working electrode

2.5 mg of the catalyst and 60 μL of 5 wt.% Nafion were dispersed in a 940 μL deionized water/ethanol solution ($v_{\text{deionized water}}$:$v_{\text{ethanol}}$ = 3:1) by sonicating for 30 min to obtain a homogeneous catalyst ink. Then, 250 μL of the ink was dropped onto a 1 cm × 1 cm carbon paper and dried at 80 °C for 2 h. The catalyst loaded on CP is 0.6 mg·cm^{-2}.

2.7 Electrochemical nitrate reduction to ammonia

The ammonia-synthesis evaluations of electrocatalysts were conducted by using a CHI 660E electrochemical workstation on an H-cell, in which cathode and anode were separated by a proton exchange membrane (Nafion 117). In the three-electrode system, CPs carrying catalysts were used as the working electrode, the silver–silver chloride electrode ($E_{Ag/AgCl}^{\ominus}$ = 0.198 V) as the reference electrode, and the platinum mesh (0.5 cm × 0.5 cm) as the counter electrode. A mixed solution of 1.0 M KOH and 1.0 M KNO_3 was used as the electrolyte in both anode and cathode chambers. During the test, the magnetic stirring in the cathode chamber reaches 1000 rpm. The measured potential was converted to E_{RHE} (E_{RHE} refers to the potential relative to the RHE) through the Nernst equation ($E_{RHE} = E_{Ag/AgCl}^{\ominus} + 0.0592 \times pH + 0.199$). The performance of each sample's ammonia synthesis was tested at least twice.

2.8 Catalyst characterization

The field emission scanning electron microscope (ZEISS, GeminiSEM 300, Germany) was used to characterize the morphology of carbon materials at an acceleration voltage of 5 kV. The high-resolution transmission electron microscopy (HRTEM) (FEI, Tecnai G2 F20, USA) operating at an acceleration voltage of 200 keV was utilized to observe the micro-morphology of the catalyst. The crystal structure of the catalyst was studied by using a powder X-ray diffractometer (Bruker AXS D8 Focus) with Cu Kα radiation (λ = 0.154 nm). The pore structure analysis was performed using a Micromeritics TriStar-II 3020 BET analyzer. Normal and *in-situ* Raman scattering spectra were performed using a reflective Renishaw Raman microscope with an excitation wavelength of 532 nm. The X-ray photoelectron spectroscopy (XPS) measurement was carried out using a VG-Multi-lab2000 X-ray photoelectron spectrometer with Mg Kα radiation ($h\nu$ = 1253.6 eV). All element spectra were calibrated with the C 1s peak (284.8 eV) as the standard.

2.9 ^{1}H nuclear magnetic resonance spectroscopy (^{1}H NMR)

After electrolysis at 200 mA·cm^{-2} for 5 h, the electrolyte was adjusted to pH = 7 with 1 M H_2SO_4 and freeze-dried. The corresponding white solid was dissolved in deionized water and made into an aqueous solution with a concentration of 20 mg·mL^{-1}. 1.0 mL of the above solution was uniformly mixed with 0.2 mL ^{2}H-dimethyl sulfoxide (DMSO) as the detection solution. In a similar way, the detection solution was prepared using the electrolyte before electrolysis. ^{1}H NMR tests were performed by Bruker Plus 600 MHz nuclear magnetic resonance spectrometer.

2.10 Measurement and calculation of electrochemical active surface area (ECSA)

Cyclic voltammetry (CV) scans were performed at different sweep rates (10–60 mV·s^{-1}). Estimate the double-layer capacitance (C_{dl}) of the catalysts according to the corresponding CV curves, and on this basis, use the following formula to calculate the ECSA of the catalysts

$$\text{ECSA} = C_{dl}/C_s \quad (1)$$

where C_s is the characteristic capacitance value of the material, which is conventionally set as 60 μF·cm^{-2}.

2.11 *In-situ* Raman spectra

In-situ Raman spectra were carried out in a three-electrode flow electrochemical cell with a quartz window (Gaussian C031-3). The reference electrode was Ag/AgCl and the counter electrode was a graphite rod. 20 μL of ink was dropped on a 2 cm × 2 cm carbon paper. After drying, it was used as the working electrode. The electrolyte components were 1 M KNO_3 and 1 M KOH. A 532 nm laser (100%), an 1800 g·mm^{-1} grating and a 50× telephoto objective were employed for sample focusing and observation. The test range was 400–2000 cm^{-1} and the acquisition time was 10 s.

2.12 *In-situ* Fourier transform infrared spectroscopy

The catalyst was treated for 50 min under one atmospheric pressure of 95% N_2, 5% NO, and 5 ppm O_2. The infrared absorption image was recorded once every 5 min using a SHIMADZU infrared spectrometer (RTracer-100) over 4000–400 cm^{-1}.

2.13 Theoretical calculations based on density functional theory (DFT)

All structural optimizations and energy calculations in this study were performed using the Vienna *ab-initio* simulation package

(VASP) based on spin-polarized density functional theory. The projected augmented wave method with a cutoff energy of 500 eV and the Perdew–Burke–Ernzerhof functional in the generalized gradient approximation (GGA) were employed. The convergence tolerances for energy and force per atom were less than 10^{-5} eV and 0.02 eV·Å^{-1}, respectively. To ensure the reliability of the calculation results, we performed entropy and zero-point energy (ZPE) corrections at 298 K. The correction formula is as follows

$$\Delta G = \Delta E + \Delta \mathrm{ZPE} - T\Delta S \quad (2)$$

where ΔG refers to the Gibbs free energy change of an elementary reaction, ΔE is the DFT-computed energy difference, ΔZPE is the change in zero-point energy, T represents temperature, and ΔS is the entropy change at 298 K.

3 Results and discussion

3.1 Synthesis and structural characterizations

The schematic depiction of the general synthetic procedure for obtaining N-doped bamboo-like carbon nanotube encapsulated CuNi alloy (Cu_7Ni_3-CNT) is illustrated in Scheme 1. The alloy catalyst was synthesized using an impregnation-calcination method, in which copper chloride, nickel chloride and melamine were mixed in ethanol to obtain the precursors. The prepared precursors were mixed and calcined with additional melamine at 800 °C in an Ar atmosphere to synthesize bamboo-like Cu_7Ni_3-CNT catalyst. By adjusting the Cu/Ni ratio, a series of alloy catalysts with different morphologies of carbon substrates (labeled as Cu_xNi_{10-x}-CN) were obtained.

The morphology and microscopic structure of Cu_7Ni_3-CNT were accurately characterized utilizing scanning electron microscopy (SEM) and transmission electron microscopy (TEM). The SEM image of Cu_7Ni_3-CNT (Fig. 1(a)) show that the carbon source is almost completely carbonized into carbon nanotubes and forms a regular bamboo-like structure. Figures 1(b)–1(d) and Fig. S3(c) in the Electronic Supplementary Material (ESM) are TEM and high-resolution TEM (HRTEM) images. As shown in Figs. 1(a)–1(c)), the synthesized carbon nanotubes exhibit uniform thickness, with an average diameter of approximately 60 nm and a

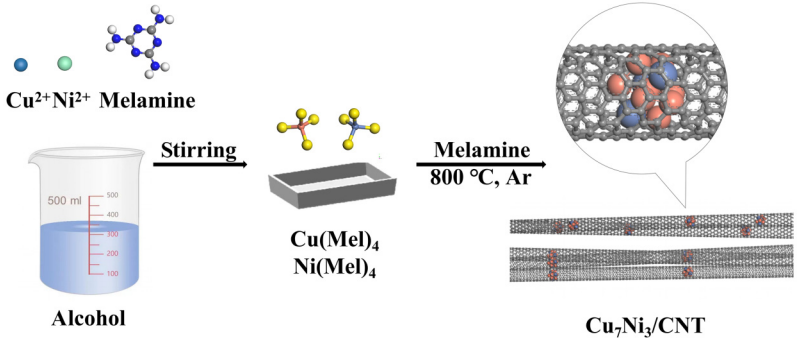

Scheme 1 Schematic procedures for the fabrication of Cu_7Ni_3-CNT.

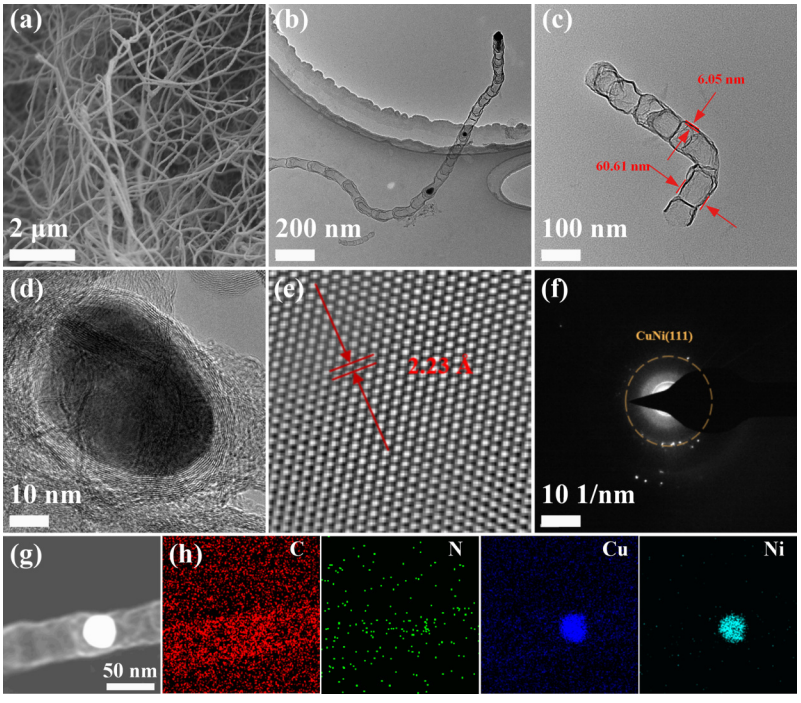

Figure 1 Morphology and microstructure characterization. (a) SEM image of Cu_7Ni_3-CNT. ((b) and (c)) TEM images of Cu_7Ni_3-CNT. (d) HRTEM image of Cu_7Ni_3-CNT. (e) HRTEM image of Cu_7Ni_3-CNT after FFT. (f) Corresponding FFT image of (d). ((g) and (h)) HAADF-STEM image of Cu_7Ni_3-CNT and corresponding elemental mapping.

wall thickness of around 6 nm, as shown in Figs. 1(b) and 1(c). The bamboo-shaped cavity is fully encapsulated with CuNi alloy, thereby providing effective protection for the catalyst. In addition, the CuNi alloy NPs exhibit a homogeneous distribution with an average particle size of approximately 20 nm (Fig. 1(d) and Fig. S3(c) in the ESM). Figure 1(e) is the image of Fig. 1(d) after fast FT (FFT), with a crystal plane spacing of 2.23 Å, corresponding to (111) crystal plane of the face-centered cubic (FCC) unit cell of Cu_7Ni_3 alloy NPs. Figure 1(f) is the corresponding FFT diagram of Fig. 1(d), indicating that the alloy particles mainly expose Cu_7Ni_3 (111) crystal plane. Figures 1(g) and 1(h) are high-angle annular dark-field scanning TEM (HAADF-STEM) of Cu_7Ni_3-CNT and corresponding elemental mapping. As can be seen from Fig. 1(h), the Cu and Ni atoms are fully mixed and evenly distributed, proving the generation of Cu_7Ni_3 alloy NPs.

X-ray photoelectron spectroscopy was performed to identify the surface chemical properties of materials. Figure S1(a) in the ESM displays the survey XPS spectra of Cu_7Ni_3-CNT, Cu-CN, and Ni-CN. Figure S1(b) in the ESM displays the high-resolution C 1s spectra of Cu_7Ni_3-CNT. The peaks observed at 284.80, 286.16, and 290.18 eV are attributed to C–C, C=C, and C–N bonds [39]. Figure 2(a) shows the high-resolution Cu 2p spectra of Cu_7Ni_3-CNT and Cu-CN. The peaks observed at 932.92 and 952.82 eV for Cu_7Ni_3-CNT are attributed to $2p_{1/2}$ and $2p_{3/2}$ of Cu^0, while the peaks at 932.58 and 952.48 eV for Cu-CN are attributed to Cu^0 $2p_{1/2}$ and $2p_{3/2}$ 36. The introduction of Ni results in a shift of the Cu^0 binding energy to higher values, thereby adjusting electronic structure of the Cu and improving the activity of catalyst. Figure 2(b) is Cu_7Ni_3-CNT and Ni-CN's high-resolution spectra of Ni 2p. The peaks observed at 855.15 and 872.54 eV for Cu_7Ni_3-CNT correspond to the $2p_{1/2}$ and $2p_{3/2}$ states of Ni^0 [34], whereas the peaks at 855.04 and 872.45 eV for Ni-CN are attributed to the same electronic states of Ni^0. The peaks at 859.25 and 876.74 eV are attributed to $2p_{1/2}$ and $2p_{3/2}$ of Ni^{2+}, indicating the presence of a few nickel precursors that have not undergone sufficient reduction. Compared with Ni-CN, alloying promotes the agglomeration of metals of Cu_7Ni_3-CNT and inhibits the formation of metal ions effectively. Figure 2(c) presents the high-resolution N 1s spectra of Cu_7Ni_3-CNT and Cu-CN. The peaks observed at 399.01, 401.19, and 404.52 eV for Cu_7Ni_3-CNT are attributed to pyridinic N, pyrrolic N, and oxidation N, while the peaks at 397.52 and 398.81 eV for Cu-CN correspond to Cu–N and pyridinic N. The introduction of Ni induces substantial alterations in N species and facilitates the conversion of Cu–N to Cu–Cu/Cu–Ni, as well as the aggregation of metals.

To further clarify the local coordination structure of Cu and Ni, X-ray absorption spectroscopy (XAS) was measured using a synchrotron radiation X-ray source. In the X-ray absorption near-edge structure (XANES) at the Cu K-edge (Fig. 2(d)), the XANES of Cu_7Ni_3-CNT is only slightly higher than that of Cu foil, which means that the coordination structure of Cu in Cu_7Ni_3-CNT is

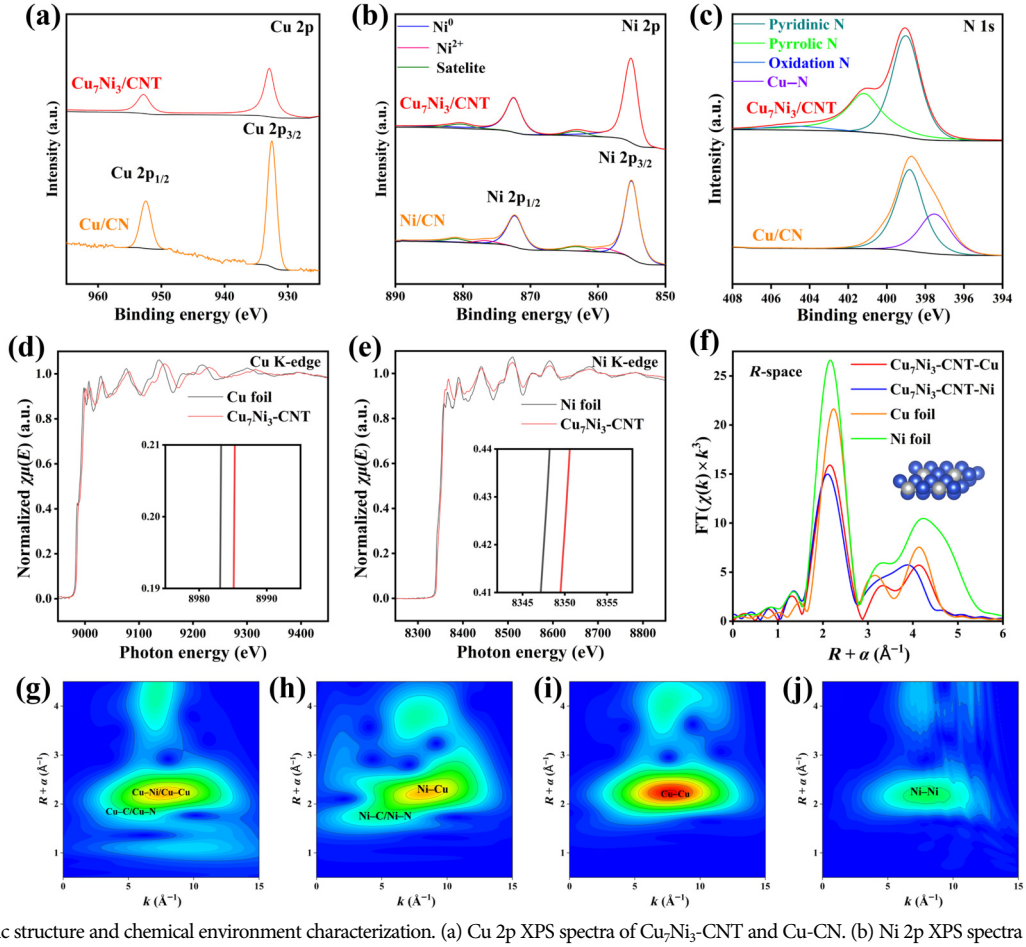

Figure 2 Electronic structure and chemical environment characterization. (a) Cu 2p XPS spectra of Cu_7Ni_3-CNT and Cu-CN. (b) Ni 2p XPS spectra of Cu_7Ni_3-CNT and Ni-CN. (c) N 1s XPS spectra of Cu_7Ni_3-CNT and Cu-CN. (d) Normalized Cu K-edge X-ray absorption near-edge structure spectra of Cu_7Ni_3-CNT and Cu foil. (e) Normalized Ni K-edge XANES of Cu_7Ni_3-CNT and Ni foil. (f) k^3-weighted FT-EXAFS and ((g)–(j)) k^3-weighted WT-EXAFS at Cu K-edge of Cu_7Ni_3-CNT, and Cu foil and Ni K-edge of Cu_7Ni_3-CNT and Ni foil.

close to metallic Cu in Cu foil. Similarly, in the X-ray absorption near-edge structure at the Ni K-edge (Fig. 2(e)), the XANES spectrum of Cu_7Ni_3-CNT is only marginally higher than that of Ni foil, indicating that the coordination environment of Ni in Cu_7Ni_3-CNT closely resembles that of metallic Ni in Ni foil. Moreover, as can be seen from the inset of XANES, during the process of compounding with CNT, electrons are transferred from metal atoms to CNT. The Fourier transform Cu and Ni K-edge extended X-ray absorption fine structure (EXAFS) was used to detect the coordination environment of Cu and Ni atoms in Cu_7Ni_3-CNT. By analyzing their extended X-ray absorption fine structure spectra, the EXAFS fitting curves of Cu_7Ni_3-CNT, Cu foil, and Ni foil at Cu *K*-space, Cu *R*-space, Ni *K*-space, and Ni *R*-space with k^3-weighted were obtained respectively, as shown in Fig. S2 in the ESM. In *R*-space (Fig. 2(f)), the peak of Cu foil at about 2.525 Å corresponds to the backscattering of the Cu–Cu first coordination shell. The peak of Ni foil at about 2.485 Å corresponds to the backscattering of the Ni–Ni first coordination shell. In the Cu *R*-space of Cu_7Ni_3-CNT, the peaks observed at approximately 2.576, 2.519, and 1.881 Å correspond to the backscattering from the first coordination shells of Cu–Ni, Cu–Cu, and Cu–N/Cu–C. In the Ni *R*-space of Cu_7Ni_3-CNT, the peaks at about 2.576 and 1.870 Å correspond to the backscattering of the Ni–Cu and Ni–N/Ni–C first coordination shell, and there is an absence of a peak at about 2.484 Å corresponding to the backscattering from the first coordination shell of Ni–Ni interactions. These results demonstrate the successful alloying of the two metal atoms and indicate a high dispersion of Ni within Cu. The k^3-weighted wavelet transform (WT) EXAFS at Cu and Ni K-edge of Cu_7Ni_3-CNT are basically the same as that of Cu and Ni foil, respectively, as shown in Figs. 2(g)–2(j). In general, EXAFS and XANES further confirm the successful synthesis of the Cu_7Ni_3 alloy structure supported by nitrogen-doped carbon nanotubes.

The structure of the catalyst was further determined through powder X-ray diffraction (XRD) measurement. As shown in Fig. 3(a), a series of XRD patterns of the catalyst reveals that the peaks belonging to the crystal planes (111), (200), and (220) of the alloy NPs are positioned between those of FCC Cu and FCC Ni, specifically at their respective positions for (111), (200), and (220). The above results once again demonstrate the successful synthesis of homogeneous CuNi alloy NPs. The incorporation of Ni induces lattice distortion in the face-centered cubic unit cell of Cu, thereby

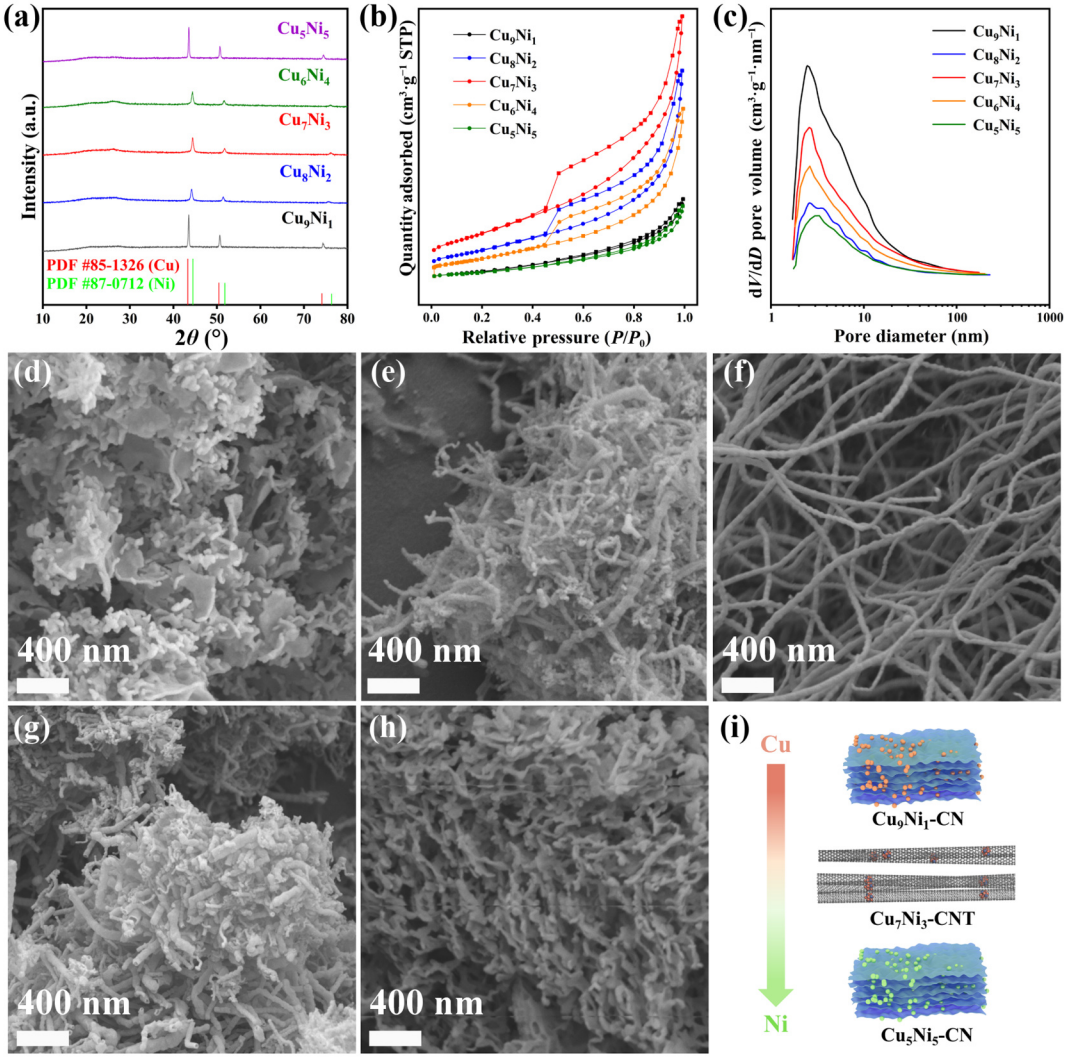

Figure 3 Structural characterization of catalysts with different copper-nickel ratios. (a) XRD patterns, (b) isothermal adsorption curves, (c) Barret–Joyner–Halenda pore size distribution. ((d)–(h)) SEM images of Cu_9Ni_1-CN, Cu_8Ni_2-CN, Cu_7Ni_3-CNT, Cu_6Ni_4-CN, and Cu_5Ni_5-CN. (i) The morphology of carbon evolving with the CuNi ratio.

changing the interplanar spacing. This phenomenon is evidenced by the peak shifts observed in the XRD patterns. Additionally, the XRD patterns of alloy crystals with different CuNi ratios also exhibit shifts.

The XRD patterns exhibit significant variations in intensity among different catalysts, indicating substantial changes in the size of nanoparticles. The morphology of the catalysts was examined using TEM to characterize the variations in Cu/Ni ratios (Fig. S3 in the ESM). The TEM images reveal that as the Cu/Ni ratio decreases from 9:1 to 5:5, the size of nanoparticles exhibits a trend of initial decrease followed by subsequent increase. The particle size can reach 100 nm when the copper-nickel ratio is 9:1 and 5:5, as indicated by the corresponding XRD data. In addition, the carbon layer is disordered, and there is no formation of regular carbon nanotubes (Figs. S3(a) and S3(e) in the ESM). The Cu_7Ni_3-CNT possesses a homogeneous particle size of approximately 20 nm and is concurrently coated with bamboo-like CNT. Therefore, it can be inferred that CNT is conducive to the dispersion of metals. The Raman spectra of Cu_7Ni_3-CNT (Fig. S4 in the ESM) indicate that the area ratio of the peaks corresponding to carbon defects and graphenic carbon (I_D and I_G) is 0.97, suggesting a significant presence of defect sites on the CNTs. These defects are advantageous for metal dispersion and enhance the hydrophilicity of CNTs.

The Brunauer–Emmett–Teller (BET, Fig. 3(b)), Barrett–Joyner–Halenda (BJH, Fig. 3(c)), and SEM (Figs. 3(d)–3(h)) images depict different ratios of alloy catalysts unveiled the influence of the metal feeding ratio on the morphology of nitrogen-doped carbon. The morphology of the carbon support transitions from lamellar to carbon nanotubes and then back to lamellar as the ratio of Cu/Ni decreases. The process of the morphology of this aforementioned phenomenon can be deduced due to the higher bond energy of Ni–C compared to that of Cu–C, rendering the surface of Ni more conducive for the formation of CNTs. The carbon yield ratio during the calcination process increases as the Ni content rises (Table S1 in the ESM). Moreover, when the feed ratio (Cu:Ni) ranges from 1:1 to 1:15, there is a continuous increase in the proportion of CNTs until nearly only carbon nanotubes remain. However, the complexation ability of melamine with Ni^{2+} is significantly weaker compared to that of Cu^{2+}, thereby resulting in a continuous reduction of melamine trapped by metal ions during precursor synthesis as the proportion of Ni increases. The reduction of carbon source leads to less carbon dissolved into the metal during the carbonization process, making it difficult to precipitate in large quantities in the form of CNTs after saturation, as shown in Fig. 3(i).

3.2 Evaluation of ammonia synthesis performance

The ammonia synthesis performance test was carried out in electrolyte of 1 M KNO_3 and 1 M KOH. The test was conducted in a typical three-electrode system in an H-cell with a Nafion 117 membrane. Spectrophotometry was employed for accurate quantification of ammonia in the electrolyte after electrolysis, and its standard curve is shown in Fig. S5 in the ESM, which exhibits a remarkable linear correlation. Figures S8, S10, and S12 in the ESM are linear sweep voltammetry (LSV) diagrams of different catalysts. The solid line represents the LSV curve in the presence of nitrate, while the dotted line corresponds to the LSV curve in its absence. It is evident that the current significantly increases upon the introduction of nitrate, thereby confirming its participation in the electrode reaction. Compared with other catalysts. Cu_7Ni_3-CNT reveals the highest ammonia production rate and Faraday efficiency at −0.8 V vs. RHE (Fig. 4(a) and Fig. S6 in the ESM), and the smallest Tafel slope (Fig. S8(b) in the ESM). This can be attributed to several factors, including the presence of a larger specific surface area due to an increased number of CNT structures, improved dispersion of metals, and consequently more exposed active sites. The ammonia synthesis performance of Cu_7Ni_3-CNT at different potentials (−0.4, −0.6, −0.8, −1.0, and −1.2 V vs. RHE) was also investigated (the corresponding current–time (*i*–*t*) image is displayed in Fig. S7 in the ESM), as shown in Fig. 4(b). Cu_7Ni_3-CNT possesses the highest Faraday efficiency (99.18%) at −0.8 V vs. RHE, accompanied by an ammonia production rate of 20.90 $mg{\cdot}cm^{-2}{\cdot}h^{-1}$; at −1.0 V vs. RHE, it achieves the maximum ammonia production rate of 23.21 $mg{\cdot}cm^{-2}{\cdot}h^{-1}$, along with a high Faraday efficiency of 90.80%. Catalysts synthesized at varying temperatures and melamine feed amounts were evaluated, as illustrated in Figs. S9 and S11 and Tables S2 and S3 in the ESM. Cu_7Ni_3-CNT with a calcination temperature of 800 °C with a precursor to melamine mass ratio of 1:10, exhibited the highest ammonia synthesis performance. The fitting results for the electrochemical active surface area of a series of catalysts at different scanning rates were derived from processing the CV images (Fig. S13 in the ESM), as shown in Fig. 4(c). The ECSAs of electrocatalysts are 49.0, 526.5, 569.0, 347.5, and 100.3 cm^2/cm^2, respectively. The ECSA of Cu_7Ni_3-CNT is maximized due to the inherently specific surface area of CNTs, which enhances their capacity for metal dispersion.

^1H nuclear magnetic resonance spectroscopy was employed to elucidate the source of nitrogen in synthetic ammonia production. Electrolysis was conducted for 10 h at a current density of 200 $mA{\cdot}cm^{-2}$, utilizing Cu_7Ni_3-CNT as the catalyst and 1 M $K^{15}NO_3$ along with 1 M KOH as the electrolyte. Following the pretreatment and testing protocols detailed in the supporting information, the ^1H NMR spectra of the electrolyte before and after electrolysis, as well as that of $^{15}NH_4Cl$, were obtained, as shown in Fig. 4(d). After 10 h of electrolysis, three distinct peaks corresponding to $^{15}NH_3/^{15}NH_4^+$ emerged near 7.0 ppm in the spectrum, indicating that nitrate serves as the source of NH_3-N. Ion chromatography (IC) was introduced to validate the Faraday efficiency determined by spectrophotometry. As shown in Fig. 4(e), the Faraday efficiencies obtained via ultraviolet–visible (UV–vis) and IC are 99.18% and 97.82%, respectively, with a mere difference of 1.36%. This confirms the reliability of the ammonia synthesis performance derived from spectrophotometric measurements. The practical applicability of the material depends on the stability of the catalyst. Hence, the stability of catalyst was subjected to testing (Fig. 4(g)). Under conditions where the initial potential of copper foam is comparable to that of Cu_7Ni_3-CNT (−1.127 V vs. RHE), an increase in overpotential of 653 mV (56.46%) is observed after only 15 h of operation at a high industrial current density of 300 $mA{\cdot}cm^{-2}$. In contrast, after nearly 400 h of stable operation at the same current density, Cu_7Ni_3-CNT exhibits only a modest increase in overpotential of 144 mV (approximately 12.45%), which can be attributed to the protective effect provided by the carbon nanotubes enveloping the alloy NPs. CNT can effectively prevent the alloy from direct contact with the electrolyte and significantly suppresses the passivation on the alloy surface. After 30 cycles at −0.8 V vs. RHE, it can still maintain a high FE (85.29%, Fig. 4(h)), and Fig. S14 in the ESM is the *i*–*t* image obtained during this process. The

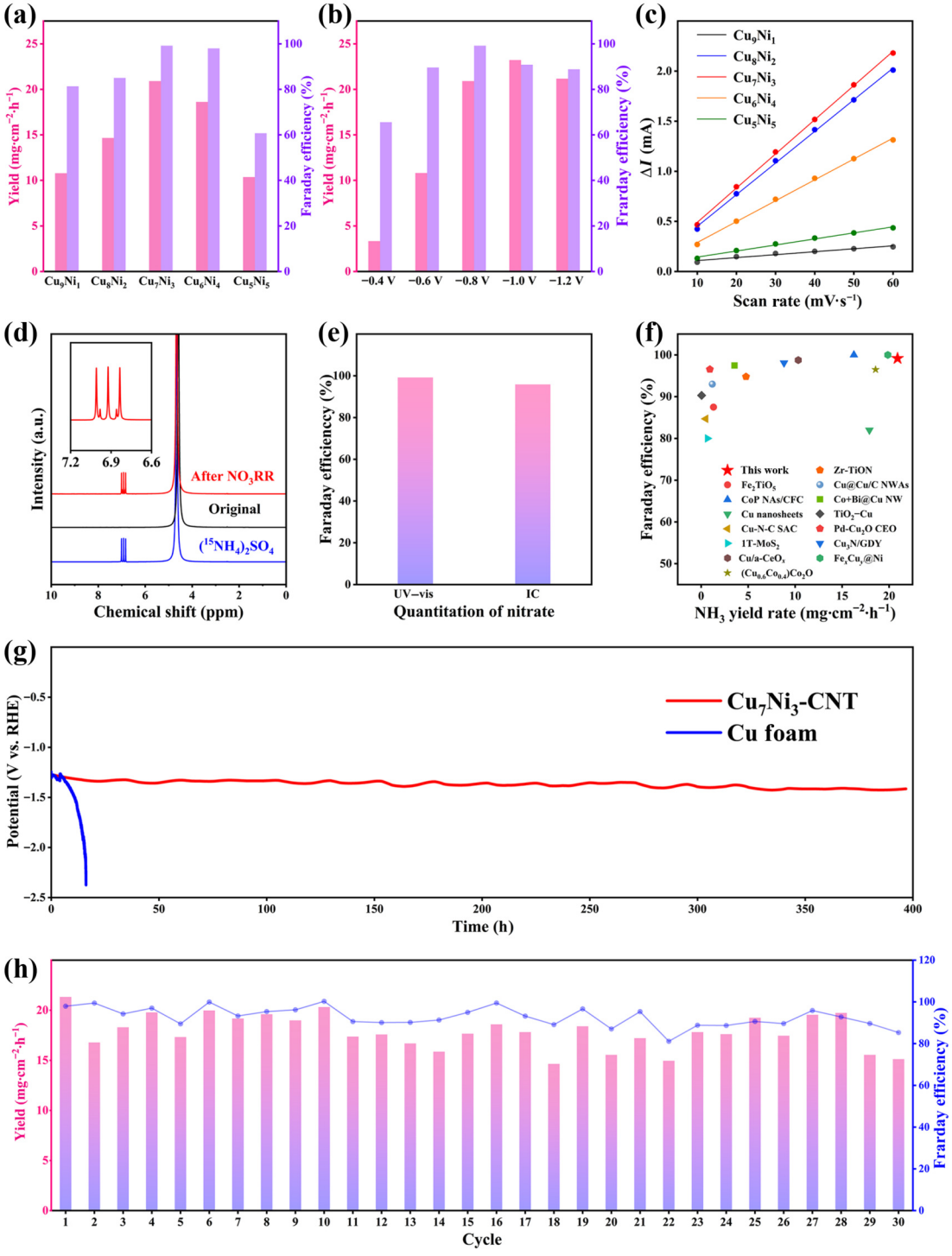

Figure 4 Electrochemical tests. (a) Ammonia synthesis performance of Cu_9Ni_1-CN, Cu_8Ni_2-CN, Cu_7Ni_3-CNT, Cu_6Ni_4-CN, and Cu_5Ni_5-CN. (b) Ammonia synthesis performance of Cu_7Ni_3-CNT at −0.4, −0.6, −0.8, −1.0, and −1.2 V vs. RHE. (c) ECSA fitting results of Cu_9Ni_1-CN, Cu_8Ni_2-CN, Cu_7Ni_3-CNT, Cu_6Ni_4-CN, and Cu_5Ni_5-CN. (d) ^1H NMR spectra of the electrolyte after ammonia synthesis with $K^{15}NO_3$. (e) Comparison of Faraday efficiency obtained by UV–vis spectroscopy and ion chromatography. (f) Comparison of ammonia synthesis performance between this work and several recent reports. (g) Long-term *V*–*t* (*V* represents potential) tests of Cu_7Ni_3-CNT and Cu foam at 300 mA·cm^{-2} for stability evaluation. (h) Ammonia synthesis performance fluctuates over 30 cycles.

electrochemical impedance spectroscopy (EIS) of Cu_7Ni_3-CNT indicates its extremely small charge transfer resistance (Fig. S15 in the ESM). Recent advancements in outstanding NO_3RR catalysts are summarized in Fig. 4(f), where Cu_7Ni_3-CNT demonstrates superior ammonia synthesis performance. Their detailed conditions and properties for ammonia synthesis are shown in Table S4 in the ESM. Consequently, CNTs enhance Cu_7Ni_3 alloy catalyst's activity, selectivity and stability for ammonia synthesis.

3.3 *In-situ* characterization and DFT theoretical calculations

Under the atmosphere of NO and O_2, *in-situ* Fourier transform

infrared spectroscopy was used to investigate to explore the enrichment phenomenon of nitrate radical inside CNTs. Figure 5(a) are *in-situ* FT-IR spectra of Cu_7Ni_3-CNT under an atmosphere comprising 95% N_2, 5% NO, and 5 ppm O_2 during 50 min. The peak at 1354 cm^{-1} is attributed to the N=O stretching vibration of NO_3^- [46–49], while the peaks at 1767 and 2335 cm^{-1} correspond to the stretching vibrations of O=C=O and C=O [45]. All these peaks are enhanced over time, indicating that nitrates are continuously generated and adsorbed on the inner surface of CNTs., which illustrates the enrichment effect of the internal space of CNTs on nitrate. To reveal the NO_3RR mechanism on the surface of Cu_7Ni_3-CNT, *in-situ* Raman spectroscopy was used to characterize the evolution mechanism of N species. As illustrated in Fig. 5(b), the peaks at 1362 and 1604 cm^{-1} correspond to the characteristic D peak and G peak of carbon materials. The peaks observed at 720, 1049, 1128, and 1519 cm^{-1} are attributed to N–O bending, free NO_3^-, $*NO_2$, and N=O from *NHO respectively [50–53]. These peaks initially intensify before subsequently diminishing as the voltage decreases. At −1.0 V vs. RHE, they exhibit their maximum intensity, correlating with the highest ammonia production. The peaks at 1281 and 1672 cm^{-1} are attributed to H–N–H wagging and $*NH_2$ vibrations, respectively [48]. Their nearly undetectable nature suggests that the hydrogenation process from *NH to $*NH_2$ and then to $*NH_3$ occurs at an extremely rapid rate. DFT calculations further substantiate this observation. The adsorption states of *H on Cu_7Ni_3 (111), Cu (111), and Ni (111) are shown in Fig. S17 in the ESM. As shown in Fig. 5(c), the ΔG_{H^*} on Cu_7Ni_3 (111) increases from −0.96 to −0.80 eV upon the incorporation of Ni. This indicates that the H* generated by water dissociation exhibits enhanced reactivity, significantly lowering the energy barriers for hydrogenation and deoxygenation of various nitrogen species. Furthermore, in the free energy diagrams of NO_3RR elementary steps for Cu_7Ni_3 (111), Cu (111), and Ni (111) (Fig. 5(h)), the incorporation of Ni results in a reduction of the energy barrier for the rate-controlling step ($*NH \rightarrow *NH_2$) of NO_3RR on Cu_7Ni_3 (111) from 0.44 to 0.96 eV. Thus, the incorporation of Ni enhances the activity of H* on the Cu_7Ni_3 (111) crystal plane, significantly accelerating the hydrogenation and deoxygenation process on the catalyst surface and ultimately improving the intrinsic activity of ammonia synthesis. The adsorption model of nitrate on Cu_7Ni_3 (111) and Cu (111) along with the differential charge density images before and after adsorption (Figs. 5(d)–5(g)), reveals the distinct adsorption structures of nitrate on the (111) crystal plane. One of the oxygen atoms in nitrate on Cu (111) forms a Cu–O bond with Cu, while the other oxygen atom establishes two Cu–O bonds with two additional copper atoms, resulting in an excessively strong adsorption state. During the adsorption process on Cu_7Ni_3 (111), only one Cu–O bond and one Ni–O bond are formed, with the change in Gibbs free energy of adsorption from −0.81 to −0.68 eV. Correspondingly, this weaker adsorption facilitates the subsequent hydrogenation and deoxygenation process, leading to a reduction in the energy barrier for $*NO_2 \rightarrow *NO$ from 0.14 to −0.13 eV. Through these analyses of *in-situ* Raman spectrum and DFT theoretical calculations of the intermediate state during the

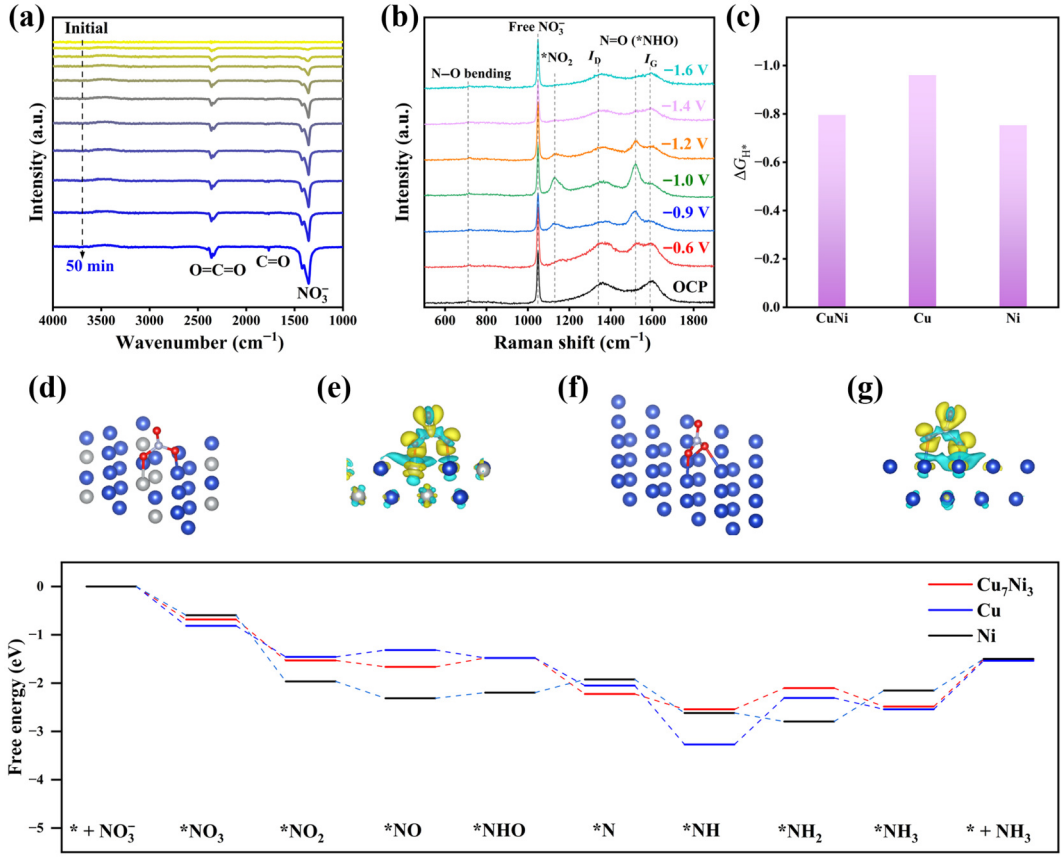

Figure 5 *In-situ* characterization and DFT theoretical calculations. (a) *In-situ* Fourier transform infrared spectroscopy of Cu_7Ni_3-CNT under the atmosphere of 95% N_2, 5% NO, and 5 ppm O_2 during 50 min. (b) *In-situ* Raman spectra of Cu_7Ni_3-CNT at different potentials. (c) ΔG_{H^*} of Cu_7Ni_3 (111), Cu (111), and Ni (111). ((d)–(g)) The adsorption model of nitrate on Cu_7Ni_3 (111) and Cu (111) and differential charge density images before and after adsorption. (h) Free energy diagrams of NO_3RR elementary steps for Cu_7Ni_3 (111), Cu (111), and Ni (111).

reduction process (Figs. S19–S21 in the ESM), the elementary steps of NO_3RR on Cu_7Ni_3 (111) can be inferred as follows: * + NO_3^- → *NO_3 → *NO_2 → *NO → *NHO → *N → *NH → *NH_2 → *NH_3 → * + NH_3 (Fig. 5(h)).

4 Conclusion

In summary, a series of alloy catalysts with varying Cu/Ni ratios have been prepared using impregnation and calcination method for the electrocatalytic NO_3RR. Compared with other alloy catalysts, Cu_7Ni_3-CNT exhibits superior performance in ammonia synthesis: It demonstrates the highest Faraday efficiency (99.18%) at −0.8 V vs. RHE, along with an impressive ammonia production rate of 20.90 mg·cm^{-2}·h^{-1}; at −1.0 V vs. RHE. The Cu_7Ni_3-CNT also achieves the highest ammonia production rate (23.21 mg·cm^{-2}·h^{-1}), accompanied by a remarkable FE of 90.80%. It is attributed to the fine adjustment of the CuNi ratio. On the one hand, under this ratio, melamine is almost completely converted into bamboo-like CNTs, resulting in a larger specific surface area for Cu_7Ni_3-CNT and enhanced ability to disperse metals, thereby exposing more active sites. *In-situ* FT-IR reveals the process in which nitrate is enriched in the inner space of CNT and is reduced on the surface of alloy nanoparticles. On the other hand, *in-situ* Raman spectroscopy and DFT calculations reveal that the incorporation of Ni weakens the excessively strong adsorption of *NO_3 and enhances the activity of *H, significantly accelerating the hydrogenation and deoxygenation process on the surface, thereby improving the NO_3RR ammonia synthesis performance on the alloy surfaces.

Electronic Supplementary Material: Supplementary material (reagents and materials, synthesis of catalysts, material characterization, product analysis, theoretical calculations, inductively coupled plasma-optical emission spectroscopy (ICP-OES) results of samples, TEM images of samples, XPS spectra of samples, Raman spectrum of sample, UV–vis standard curve and corresponding UV–vis spectrum, catalytic performance of samples, LSV curves of samples, *i*–*t* curves of samples, EXAFS fitting curves of samples, EIS, CV, and ECSA curves of samples, polarization curves of samples, and optimized structures for DFT calculations) is available in the online version of this article at https://doi.org/10.26599/NR.2025.94907265.

Data availability

All data needed to support the conclusions in the paper are presented in the manuscript and the Electronic Supplementary Material. Additional data related to this paper may be requested from the corresponding author upon request.

Acknowledgements

The authors gratefully acknowledge the financial support from the National Natural Science Foundation of China (Nos. 22035009 and 22122113). We thank Quantum Design (Beijing) Co., Ltd. for their assistance with X-ray absorption spectroscopy measurements, as well as support throughoutthe data processing and analysis phases.

Declaration of competing interest

The authors declare that they have no known competing financial interests or personal relationships that could have appeared to influence the work reported in this paper.

Author contribution statement

G. H. J.: Conceptualization, data curation, formal analysis, methodology, validation, visualization, writing – original draft, writing – review & editing. Y. Q. S.: Supervision, formal analysis, writing – review & editing, project administration. P. L. L.: Methodology, formal analysis. J. Q. L.: Software, conceptualization. P. Z.: Formal analysis. Y. C. W.: Methodology. W. Y. S.: Methodology. Z. X. L.: Supervision, formal analysis. Z. Z.: Methodology. J. L.: Supervision, methodology, funding acquisition. All the authors have approved the final manuscript.

Use of AI statement

None.

References

[1] Xu, H.; Ma, Y. Y.; Chen, J.; Zhang, W. X.; Yang, J. P. Electrocatalytic reduction of nitrate—A step towards a sustainable nitrogen cycle. *Chem. Soc. Rev.* **2022**, *51*, 2710–2758.

[2] Morlanés, N.; Katikaneni, S. P.; Paglieri, S. N.; Harale, A.; Solami, B.; Sarathy, S. M.; Gascon, J. A technological roadmap to the ammonia energy economy: Current state and missing technologies. *Chem. Eng. J.* **2021**, *408*, 127310.

[3] Zhang, X.; Wang, Y. T.; Liu, C. B.; Yu, Y. F.; Lu, S. Y.; Zhang, B. Recent advances in non-noble metal electrocatalysts for nitrate reduction. *Chem. Eng. J.* **2021**, *403*, 126269.

[4] Chen, W. D.; Yang, X. Y.; Chen, Z. D.; Ou, Z. J.; Hu, J. T.; Xu, Y.; Li, Y. L.; Ren, X. Z.; Ye, S. H.; Qiu, J. S. et al. Emerging applications, developments, prospects, and challenges of electrochemical nitrate-to-ammonia conversion. *Adv. Funct. Mater.* **2023**, *33*, 2300512.

[5] Huang, Z. L.; Rafiq, M.; Woldu, A. R.; Tong, Q. X.; Astruc, D.; Hu, L. S. Recent progress in electrocatalytic nitrogen reduction to ammonia (NRR). *Coord. Chem. Rev.* **2023**, *478*, 214981.

[6] Mou, T.; Wang, Y. T.; Deák, P.; Li, H.; Long, J.; Fu, X. Y.; Zhang, B.; Frauenheim, T.; Xiao, J. P. Predictive theoretical model for the selective electroreduction of nitrate to ammonia. *J. Phys. Chem. Lett.* **2022**, *13*, 9919–9927.

[7] Martínez, J.; Ortiz, A.; Ortiz, I. State-of-the-art and perspectives of the catalytic and electrocatalytic reduction of aqueous nitrates. *Appl. Catal. B: Environ.* **2017**, *207*, 42–59.

[8] Chen, W. D.; Xu, Y.; Liu, J. X.; Cao, H. Q.; Li, Y. L.; Ren, X. Z.; Ye, S. H.; Liu, J. H.; Zhang, Q. L. Recent developments in Ti-based nanocatalysts for electrochemical nitrate-to-ammonia conversion. *Inorg. Chem. Front.* **2023**, *10*, 4901–4917.

[9] Garcia-Segura, S.; Lanzarini-Lopes, M.; Hristovski, K.; Westerhoff, P. Electrocatalytic reduction of nitrate: Fundamentals to full-scale water treatment applications. *Appl. Catal. B: Environ.* **2018**, *236*, 546–568.

[10] Zhou, M.; Wang, H. L.; Guo, S. J. Towards high-efficiency nanoelectrocatalysts for oxygen reduction through engineering advanced carbon nanomaterials. *Chem. Soc. Rev.* **2016**, *45*, 1273–1307.

[11] Yu, L.; Deng, D. H.; Bao, X. H. Chain mail for catalysts. *Angew. Chem., Int. Ed.* **2020**, *59*, 15294–15297.

[12] Song, Y.; Yang, X.; Liu, H.; Liang, S. X.; Cai, Y. F.; Yang, W. Q.; Zhu, K. X.; Yu, L.; Cui, X. J.; Deng, D. H. High-pressure electro-Fenton driving CH_4 conversion by O_2 at room temperature. *J. Am. Chem. Soc.* **2024**, *146*, 5834–5842.

[13] Shin, S.; Lee, E.; Nam, J.; Kwon, J.; Choi, Y.; Kim, B. J.; Ham, H. C.; Lee, H. Carbon-embedded Pt alloy cluster catalysts for proton

exchange membrane fuel cells. *Adv. Energy Mater.* **2024**, *14*, 2400599.

[14] Huang, L.; Su, Y. Q.; Qi, R. J.; Dang, D.; Qin, Y. Y.; Xi, S. B.; Zaman, S.; You, B.; Ding, S. J.; Xia, B. Y. Boosting oxygen reduction via integrated construction and synergistic catalysis of porous platinum alloy and defective graphitic carbon. *Angew. Chem., Int. Ed.* **2021**, *60*, 25530–25537.

[15] Xu, Y.; Ren, K. L.; Ren, T. L.; Wang, M. Z.; Wang, Z. Q.; Li, X. N.; Wang, L.; Wang, H. J. Ultralow-content Pd *in-situ* incorporation mediated hierarchical defects in corner-etched Cu_2O octahedra for enhanced electrocatalytic nitrate reduction to ammonia. *Appl. Catal. B: Environ.* **2022**, *306*, 121094.

[16] Chen, K.; Ma, Z. Y.; Li, X. C.; Kang, J. L.; Ma, D. W.; Chu, K. Single-atom Bi alloyed Pd metallene for nitrate electroreduction to ammonia. *Adv. Funct. Mater.* **2023**, *33*, 2209890.

[17] Xie, M. H.; Tang, S. S.; Li, Z.; Wang, M. Y.; Jin, Z. Y.; Li, P. P.; Zhan, X.; Zhou, H.; Yu, G. H. Intermetallic single-atom alloy In–Pd bimetallene for neutral electrosynthesis of ammonia from nitrate. *J. Am. Chem. Soc.* **2023**, *145*, 13957–13967.

[18] Gao, Y.; Wang, R.; Li, Y. D.; Han, E. S.; Song, M. S.; Yang, Z. Y.; Guo, F.; He, Y. Z.; Yang, X. H. Regulating dynamic equilibrium of active hydrogen for super-efficient nitrate electroreduction to ammonia. *Chem. Eng. J.* **2023**, *474*, 145546.

[19] Kim, K.; Zagalskaya, A.; Ng, J. L.; Hong, J.; Alexandrov, V.; Pham, T. A.; Su, X. Coupling nitrate capture with ammonia production through bifunctional redox-electrodes. *Nat. Commun.* **2023**, *14*, 823.

[20] Cai, J. M.; Huang, J. J.; Cao, A.; Wei, Y. Y.; Wang, H. M.; Li, X.; Jiang, Z.; Waterhouse, G. I. N.; Lu, S. Y.; Zang, S. Q. Interfacial hydrogen bonding-involved electrocatalytic ammonia synthesis on OH-terminated MXene. *Appl. Catal. B: Environ.* **2023**, *328*, 122473.

[21] Kim, K. H.; Lee, H.; Huang, X. P.; Choi, J. H.; Chen, C. P.; Kang, J. K.; O'Hare, D. Energy-efficient electrochemical ammonia production from dilute nitrate solution. *Energy Environ. Sci.* **2023**, *16*, 663–672.

[22] Wang, Y. T.; Xu, Y.; Cheng, C. Q.; Zhang, B. S.; Zhang, B.; Yu, Y. F. Phase-regulated active hydrogen behavior on molybdenum disulfide for electrochemical nitrate-to-ammonia conversion. *Angew. Chem., Int. Ed.* **2024**, *63*, e202315109.

[23] Liu, Y. T.; Qiu, W. X.; Wang, P. F.; Li, R.; Liu, K.; Omer, K. M.; Jin, Z. Y.; Li, P. P. Pyridine-N-rich Cu single-atom catalyst boosts nitrate electroreduction to ammonia. *Appl. Catal. B: Environ.* **2024**, *340*, 123228.

[24] Zhang, S.; Wu, J. H.; Zheng, M. T.; Jin, X.; Shen, Z. H.; Li, Z. H.; Wang, Y. J.; Wang, Q.; Wang, X. B.; Wei, H. et al. Fe/Cu diatomic catalysts for electrochemical nitrate reduction to ammonia. *Nat. Commun.* **2023**, *14*, 3634.

[25] Yang, J.; Qi, H. F.; Li, A. Q.; Liu, X. Y.; Yang, X. F.; Zhang, S. X.; Zhao, Q.; Jiang, Q. K.; Su, Y.; Zhang, L. L. et al. Potential-driven restructuring of Cu single atoms to nanoparticles for boosting the electrochemical reduction of nitrate to ammonia. *J. Am. Chem. Soc.* **2022**, *144*, 12062–12071.

[26] Xiao, L.; Dai, W. D.; Mou, S. Y.; Wang, X. Y.; Cheng, Q.; Dong, F. Coupling electrocatalytic cathodic nitrate reduction with anodic formaldehyde oxidation at ultra-low potential over Cu_2O. *Energy Environ. Sci.* **2023**, *16*, 2696–2704.

[27] Zhou, N.; Wang, Z.; Zhang, N.; Bao, D.; Zhong, H. X.; Zhang, X. B. Potential-induced synthesis and structural identification of oxide-derived Cu electrocatalysts for selective nitrate reduction to ammonia. *ACS Catal.* **2023**, *13*, 7529–7537.

[28] Hu, T.; Wang, C. H.; Wang, M. T.; Li, C. M.; Guo, C. X. Theoretical insights into superior nitrate reduction to ammonia performance of copper catalysts. *ACS Catal.* **2021**, *11*, 14417–14427.

[29] Liu, L. C.; Corma, A. Bimetallic sites for catalysis: From binuclear metal sites to bimetallic nanoclusters and nanoparticles. *Chem. Rev.* **2023**, *123*, 4855–4933.

[30] Chen, F. Y.; Wu, Z. Y.; Gupta, S.; Rivera, D. J.; Lambeets, S. V.; Pecaut, S.; Kim, J. Y. T.; Zhu, P.; Finfrock, Y. Z.; Meira, D. M. et al. Efficient conversion of low-concentration nitrate sources into ammonia on a Ru-dispersed Cu nanowire electrocatalyst. *Nat. Nanotechnol.* **2022**, *17*, 759–767.

[31] Chen, X. H.; Cheng, Y. M.; Zhang, B.; Zhou, J.; He, S. S. Gradient-concentration RuCo electrocatalyst for efficient and stable electroreduction of nitrate into ammonia. *Nat. Commun.* **2024**, *15*, 6278.

[32] Shao, J. Q.; Jing, H. J.; Wei, P. F.; Fu, X. Y.; Pang, L.; Song, Y. P.; Ye, K.; Li, M. R.; Jiang, L. Z.; Ma, J. Y. et al. Electrochemical synthesis of ammonia from nitric oxide using a copper-tin alloy catalyst. *Nat. Energy* **2023**, *8*, 1273–1283.

[33] Jiang, H. F.; Chen, G. F.; Savateev, O.; Xue, J.; Ding, L. X.; Liang, Z. X.; Antonietti, M.; Wang, H. H. Enabled efficient ammonia synthesis and energy supply in a zinc-nitrate battery system by separating nitrate reduction process into two stages. *Angew. Chem., Int. Ed.* **2023**, *62*, e202218717.

[34] Yu, W. Q.; Yu, J. Y.; Huang, M.; Wang, Y. J.; Wang, Y. J.; Li, J. W.; Liu, H.; Zhou, W. J. Laser-controlled tandem catalytic sites of CuNi alloys with ampere-level electrocatalytic nitrate-to-ammonia reduction activities for Zn-nitrate batteries. *Energy Environ. Sci.* **2023**, *16*, 2991–3001.

[35] Gao, W. S.; Xie, K. F.; Xie, J.; Wang, X. M.; Zhang, H.; Chen, S. Q.; Wang, H.; Li, Z. L.; Li, C. Alloying of Cu with Ru enabling the relay catalysis for reduction of nitrate to ammonia. *Adv. Mater.* **2023**, *35*, 2202952.

[36] Fang, J. Y.; Zheng, Q. Z.; Lou, Y. Y.; Zhao, K. M.; Hu, S. N.; Li, G.; Akdim, O.; Huang, X. Y.; Sun, S. G. Ampere-level current density ammonia electrochemical synthesis using CuCo nanosheets simulating nitrite reductase bifunctional nature. *Nat. Commun.* **2022**, *13*, 7899.

[37] Li, H.; Yan, C. X.; Guo, H. Y.; Shin, K.; Humphrey, S. M.; Werth, C. J.; Henkelman, G. Cu_xIr_{1-x} nanoalloy catalysts achieve near 100% selectivity for aqueous nitrite reduction to NH_3. *ACS Catal.* **2020**, *10*, 7915–7921.

[38] Wang, S.; Li, L.; Hui, K. S.; Dinh, D. A.; Lu, Z. Y.; Zhang, Q. J.; Hui, K. N. Non-noble single-atom alloy for electrocatalytic nitrate reduction using hierarchical high-throughput screening. *Nano Energy* **2023**, *113*, 108543.

[39] Zhang, Z. H.; Wu, P. Y. A facile one-pot route towards three-dimensional graphene-based microporous N-doped carbon composites. *RSC Adv.* **2014**, *4*, 45619–45624.

[40] Jiang, L. J.; Qiu, L. J.; Cen, T. L.; Liu, Y. Y.; Peng, X. M.; Ye, Z. F.; Yuan, D. S. Controllable Co@N-doped graphene anchored onto the NRGO toward electrocatalytic hydrogen evolution at all pH values. *Chem. Commun.* **2020**, *56*, 567–570.

[41] Ma, J. W.; Wang, M.; Lei, G. Y.; Zhang, G. L.; Zhang, F. B.; Peng, W. C.; Fan, X. B.; Li, Y. Polyaniline derived N-doped carbon-coated cobalt phosphide nanoparticles deposited on N-doped graphene as an efficient electrocatalyst for hydrogen evolution reaction. *Small* **2018**, *14*, 1702895.

[42] Zhao, R. Y.; Wang, Y. D.; Ji, G. P.; Zhong, J. J.; Zhang, F. T.; Chen, M. F.; Tong, S. R.; Wang, P.; Wu, Z. H.; Han, B. X. et al. Partially nitrided Ni nanoclusters achieve energy-efficient electrocatalytic CO_2 reduction to CO at ultralow overpotential. *Adv. Mater.* **2023**, *35*, 2205262.

[43] Chhetri, M.; Wan, M. Y.; Jin, Z. H.; Yeager, J.; Sandor, C.; Rapp, C.; Wang, H.; Lee, S.; Bodenschatz, C. J.; Zachman, M. J. et al. Dual-site catalysts featuring platinum-group-metal atoms on copper shapes boost hydrocarbon formations in electrocatalytic CO_2 reduction. *Nat. Commun.* **2023**, *14*, 3075.

[44] Guo, W. X.; Gao, X. P.; Zhu, M. Z.; Xu, C. X.; Zhu, X. R.; Zhao, X. Y.; Sun, R. B.; Xue, Z. G.; Song, J.; Tian, L. et al. A closely packed $Pt_{1.5}Ni_{1-x}$/Ni–N–C hybrid for relay catalysis towards oxygen reduction. *Energy Environ. Sci.* **2023**, *16*, 148–156.

[45] Gao, K.; Wang, B.; Tao, L.; Cunning, B. V.; Zhang, Z. P.; Wang, S. Y.; Ruoff, R. S.; Qu, L. T. Efficient metal-free electrocatalysts from N-doped carbon nanomaterials: Mono-doping and Co-doping. *Adv. Mater.* **2019**, *31*, 1805121.

[46] Bai, L. C.; Franco, F.; Timoshenko, J.; Rettenmaier, C.; Scholten, F.; Jeon, H. S.; Yoon, A.; Rüscher, M.; Herzog, A.; Haase, F. T. et al. Electrocatalytic nitrate and nitrite reduction toward ammonia using Cu_2O nanocubes: Active species and reaction mechanisms. *J. Am. Chem. Soc.* **2024**, *146*, 9665–9678.

[47] Wang, J. J.; Ou, Z. D.; Dong, C. B.; Su, M. Y.; Ali, A.; Kuklin, A. V.; Ågren, H.; Baryshnikov, G. V.; Liu, Y.; Zhao, X. et al. Electronic structure modulated by B-doped Cu promotes electrocatalytic nitrate reduction for ammonia production. *ACS Catal.* **2025**, *15*, 156–166.

[48] Zhao, X.; Yang, Z. Q.; Kuklin, A. V.; Baryshnikov, G. V.; Ågren, H.; Zhou, X. H.; Zhang, H. B. Efficient ambient electrocatalytic ammonia synthesis by nanogold triggered via boron clusters combined with carbon nanotubes. *ACS Appl. Mater. Interfaces* **2020**, *12*, 42821–42831.

[49] Deng, X. F.; Xia, S. Y.; Zhao, H. X.; Wang, J. J.; Wang, Z. X.; Kuklin, A.; Ågren, H.; Baryshnikov, G.; Zhang, H. B. A new strategy for boron cluster-based metal boride (Co_2B) synthesis and its applicability to electrocatalytic nitrate reduction. *Chem. Eng. J.* **2024**, *485*, 149639.

[50] Li, S. Y.; Zhang, G.; Ma, X.; Gao, H.; Fu, D. L.; Wang, T.; Zeng, J. R.; Zhao, Z. J.; Zhang, P.; Gong, J. L. Atomically isolated Pd sites promote electrochemical CO reduction to acetate through a protonation-regulated mechanism. *J. Am. Chem. Soc.* **2024**, *146*, 31927–31934.

[51] Zhang, G. K.; Li, X. T.; Chen, K.; Guo, Y. L.; Ma, D. W.; Chu, K. Tandem electrocatalytic nitrate reduction to ammonia on MBenes. *Angew. Chem., Int. Ed.* **2023**, *62*, e202300054.

[52] Liu, Y.; Niu, S. Y.; Zou, Y.; Huang, S. L.; Shi, Y. X.; Gao, S. Y.; Tsiakaras, P. Electrochemical production of ammonia: Nitrate reduction over novel Cu–Ni–Al metallic glass nanoparticles used as highly active and durable catalyst. *Appl. Catal. B: Environ. Energy* **2025**, *363*, 124729.

[53] Yao, Z. B.; Liu, S. Q.; Liu, H. H.; Ruan, Y. K.; Hong, S.; Wu, T. S.; Hao, L. D.; Soo, Y. L.; Xiong, P.; Li, M. M. J. et al. Pre-adsorbed H-assisted N_2 activation on single-atom cadmium-O_5 decorated In_2O_3 for efficient NH_3 electrosynthesis. *Adv. Funct. Mater.* **2023**, *33*, 2209843.